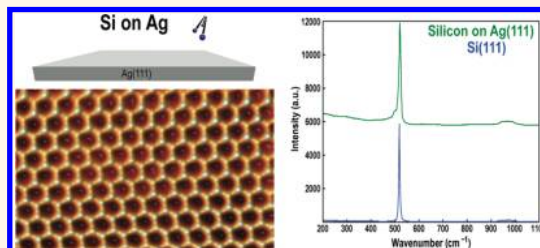


Silicon Growth at the Two-Dimensional Limit on Ag(111)

Andrew J. Mannix,^{†,*,||} Brian Kiraly,^{†,*,||} Brandon L. Fisher,[†] Mark C. Hersam,^{*,§,*} and Nathan P. Guisinger^{†,*}

[†]Center for Nanoscale Materials, Argonne National Laboratory, 9700 South Cass Avenue, Building 440, Argonne, Illinois 60439, United States, and [‡]Department of Materials Science and Engineering and [§]Department of Chemistry, Northwestern University, 2220 Campus Drive, Evanston, Illinois 60208, United States. ^{||}These authors contributed equally.

ABSTRACT Having fueled the microelectronics industry for over 50 years, silicon is arguably the most studied and influential semiconductor. With the recent emergence of two-dimensional (2D) materials (*e.g.*, graphene, MoS₂, phosphorene, *etc.*), it is natural to contemplate the behavior of Si in the 2D limit. Guided by atomic-scale studies utilizing ultrahigh vacuum (UHV), scanning tunneling microscopy (STM), and spectroscopy (STS), we have investigated the 2D limits of Si growth on Ag(111). In contrast to previous reports of a distinct sp²-bonded silicene allotrope, we observe the evolution of apparent surface alloys (ordered 2D silicon–Ag surface phases), which culminate in the precipitation of crystalline, sp³-bonded Si(111) nanosheets. These nanosheets are capped with a $\sqrt{3}$ honeycomb phase that is isostructural to a $\sqrt{3}$ honeycomb-chained-trimer (HCT) reconstruction of Ag on Si(111). Further investigations reveal evidence for silicon intermixing with the Ag(111) substrate followed by surface precipitation of crystalline, sp³-bonded silicon nanosheets. These conclusions are corroborated by *ex situ* atomic force microscopy (AFM), transmission electron microscopy (TEM), Raman spectroscopy, and X-ray photoelectron spectroscopy (XPS). Even at the 2D limit, scanning tunneling spectroscopy shows that the sp³-bonded silicon nanosheets exhibit semiconducting electronic properties.



KEYWORDS: two-dimensional materials · silicene · surface reconstruction · scanning tunneling microscopy · molecular beam epitaxy

The realization of extraordinary structural, electronic, thermal, optical, and magnetic properties in atomically thin materials such as graphene,^{1–4} hexagonal BN,⁵ and MoS₂^{6,7} has produced intense interest in the development of novel two-dimensional systems. In graphene, the superlative electronic properties are a consequence of effectively massless charge carriers known as Dirac fermions, which result from the gapless, linear carrier dispersion near the Fermi level.^{1,8} The success of graphene has stimulated the investigation of atomically layered phases formed from other group IV elements such as Si (silicene) and Ge (germanene). Computational studies suggest that silicene and germanene are stable^{9,10} and exhibit a buckled honeycomb structure in free space. In addition, silicene and germanene are predicted to exhibit Dirac fermion carriers similar to graphene,^{10,11} as well as a tunable electronic band gap¹² and exotic topological states^{13,14} that result from their higher atomic number and buckled structure.

Recent studies report the synthesis of silicene on metallic substrates including

nanoribbons on Ag(110)¹⁵ and nanosheets on Ag(111),^{16,17} Ir(111),¹⁸ and ZrB₂(0001).¹⁹ Silver has been the predominant substrate, and ultrathin silicon on Ag(111) exhibits a variety of phases that have been attributed to various buckling arrangements for the silicon atoms. Of these, the 3×3 ¹⁶ and $(\sqrt{3} \times \sqrt{3})R30^\circ$ ^{17,20–22} phases have been most extensively studied. The $(\sqrt{3} \times \sqrt{3})R30^\circ$ phase (*i.e.*, $\sqrt{3}$ -silicene) forms at the highest growth temperatures and has been observed to grow beyond a monolayer, both upon itself¹⁷ and on other phases²³ (see Figure S1, Supporting Information, for details of the reported $\sqrt{3}$ -silicene structural model). Early experiments also report evidence for Dirac fermion charge carriers^{20,21,23} and superconductivity²⁴ in this phase.

Prior to the widespread interest in free-standing two-dimensional materials, the Ag–Si system was heavily investigated in the context of Ag-driven reconstructions to various crystalline Si surfaces.^{25–28} Of these, the Ag-induced Si(111) $(\sqrt{3} \times \sqrt{3})R30^\circ$ reconstruction garnered particular interest

* Address correspondence to nguisinger@anl.gov, m-hersam@northwestern.edu.

Received for review June 2, 2014 and accepted July 5, 2014.

Published online 10.1021/nn503000w

© XXXX American Chemical Society

due to its homogeneous honeycomb structure, which was characterized as a two-dimensional electron gas^{29,30} and employed as a substrate for directed molecular self-assembly.³¹ After extensive investigation including first-principles calculations²⁶ and characterization *via* electron diffraction,²⁵ ion scattering,³² X-ray standing waves,³³ transmission electron microscopy,²⁸ and scanning tunneling microscopy (STM),²⁷ the room temperature structure of the Ag-induced Si(111)-($\sqrt{3} \times \sqrt{3}$)R30° reconstruction was described by the honeycomb chain trimer (HCT) model (shown in Figure S1, Supporting Information). Further STM work at low temperature showed the formation of domains in which the honeycomb contrast was shifted between the apparent honeycomb sublattices,²⁷ resulting in the inequivalent triangle (IET) model. The IET model was reconciled with the HCT model through proposed thermally driven fluctuations between two energy-degenerate IET configurations at elevated temperature, similar to a model proposed for $\sqrt{3}$ -silicene.²² Additionally, essentially identical ($\sqrt{3} \times \sqrt{3}$)R30° phases are observed for Au on Si(111) and Au/Ag on Ge(111).^{30,34}

Here, we thoroughly investigate the phases resulting from Si deposition on Ag(111) and demonstrate that the $\sqrt{3}$ Si phase on Ag(111) is structurally and electronically identical to HCT on Si(111) at the atomic-scale through STM characterization. Furthermore, X-ray photoelectron spectroscopy (XPS) depth profiles reveal that oxidation of the top several layers protects the underlying Si in ambient, as well as an unexpectedly high subsurface Si concentration. Cross-sectional transmission electron microscopy (TEM) confirms that formation of a surface oxide allows the Si nanosheets to survive ambient exposure. Through Raman spectroscopy, we observe vibrational modes characteristic of bulklike sp^3 Si phases, which are shown to originate from $\sqrt{3}$ phase regions through correlated atomic force microscopy (AFM). Further STM and AFM characterization shows that silicon deposition results in large areas of the $\sqrt{7} \times \sqrt{7}$ silicon phase¹⁷ (or $\sqrt{7}$ phase), which grow to nearly complete surface coverage. Upon continued silicon deposition, these regions are converted to sp^3 Si. These results suggest that surface alloying (*i.e.*, the $\sqrt{7}$ phase) occurs until a critical concentration is reached, following which bulklike Si precipitates. Therefore, the observed $\sqrt{3}$ phase consists of ultrathin slabs of diamond-cubic Si(111) crystals capped with a Ag-induced reconstruction. Significantly, scanning tunneling spectroscopy shows that the $\sqrt{3}$ phase possesses a significant bandgap, thereby overcoming one of the principal limitations imposed by the gapless nature of sp^2 -bonded two-dimensional nanomaterials.

RESULTS AND DISCUSSION

Following Si deposition at substrate temperatures from 200 to 320 °C, we observe domains in the STM

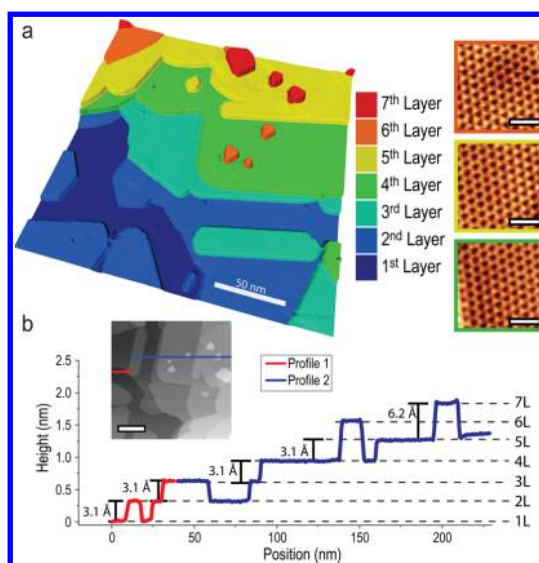


Figure 1. (a) Three-dimensional rendering of an STM topographic image of multilayer Si on Ag(111) that shows seven distinct layers, each terminated with a $\sqrt{3}$ surface reconstruction ($V_{\text{sample}} = -1.0$ V, $I_t = 400$ pA). Right side: atomic-scale STM images (scale bars = 2 nm) from the fourth layer (green frame), fifth layer (yellow frame), and sixth layer (orange frame) ($V_{\text{sample}} = -1.0$ V, $I_t = 800$ pA). (b) Line profile of the topography in (a), showing a uniform step height of 0.31 nm for monolayer-height steps and 0.62 nm for bilayer-height steps. These step heights correlate with the Si(111) interplanar spacing (inset: topography image indicating the profiled region, scale bar = 50 nm).

topography that match previous reports of various highly buckled silicon phases. The temperature-dependent evolution of the sample morphology is detailed in the Supporting Information, Figure S2. At substrate growth temperatures between 340 and 360 °C, the surface morphology is dominated by planar, edge-faceted domains. Following high Si doses on Ag(111) (*i.e.*, over two monolayers deposited), we observe multilayer $\sqrt{3}$ phase regions with as many as seven distinct layers, as illustrated by the large-area STM image rendering in Figure 1a. Atomically resolved empty states scans acquired at the fourth, fifth, and sixth layer (shown as insets) reveal a consistent honeycomb structure with a 0.64 ± 0.02 nm periodicity (*i.e.*, 0.37 ± 0.02 nm apparent interatomic spacing) matching literature reports of $\sqrt{3}$ -silicene.¹⁷ A line profile over the $\sqrt{3}$ phase domains, as in Figure 1b, reveals step heights of 0.31 nm as observed in previous studies of multilayer growth.³⁵ This value matches the Si(111) atomic step height and differs significantly from the Ag(111) atomic step height of 0.236 nm. The growth of the multilayer $\sqrt{3}$ phase is consistently observed in favor of wider surface coverage. We have also observed that the $\sqrt{3}$ phase is energetically favorable not only in the high temperature limit but also in the general presence of excess silicon. For increasingly high Si coverage (*e.g.*, over 10 monolayers), we observe the formation of $\sqrt{3}$ phase domains and faceted, anisotropic crystallites (see Figure S3, Supporting Information). Additionally,

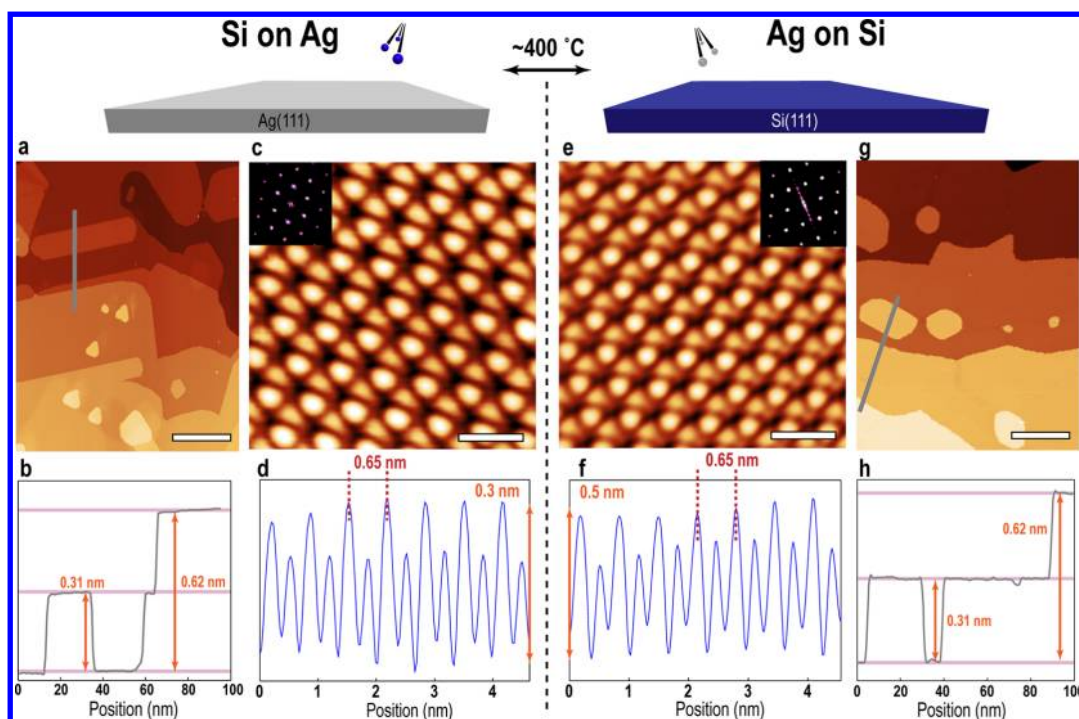


Figure 2. (Top) Growth schematic for Si on Ag(111) and Ag on Si(111). (a) STM topography of the $\sqrt{3}$ phase for Si on Ag(111) (scale bar = 50 nm, $V_{\text{sample}} = -1.0$ V, $I_t = 400$ pA) with (b) line profile revealing a 0.31 nm step height. (c) Atomic-scale STM topography of the $\sqrt{3}$ phase for Si on Ag(111) with (d) line profile (scale bar = 1 nm, $V_{\text{sample}} = 0.3$ V, $I_t = 1.0$ nA). (e) Atomic-scale STM topography of the $\sqrt{3}$ phase for Ag on Si(111) with (f) line profile (scale bar = 1 nm, $V_{\text{sample}} = -1.0$ V, $I_t = 100$ pA) revealing an indistinguishable lateral atomic periodicity compared to the $\sqrt{3}$ phase for Si on Ag(111) shown in part (d). (g) STM topography of the $\sqrt{3}$ phase for Ag on Si(111) with (h) line profile (scale bar = 50 nm, $V_{\text{sample}} = 0.85$ V, $I_t = 1.4$ nA), showing identical step heights and similar island shapes to the $\sqrt{3}$ phase for Si on Ag(111) shown in part (a).

formation of the $\sqrt{3}$ phase requires a critical threshold dose of ca. two monolayers before $\sqrt{3}$ phase domains are observed.

Figure 2 presents a direct STM comparison between Si deposition on Ag(111) and Ag deposition on Si(111). The left portion of Figure 2 details the growth of the aforementioned $\sqrt{3}$ Si phase on Ag(111). Figure 2a shows a representative STM topography image, with the associated line profile in Figure 2b demonstrating the consistent 0.31 nm step height. High-resolution empty states STM topography images, as in Figure 2c, show slight contrast in intensity between the two sublattices. The line profile, shown in Figure 2d, more clearly demonstrates this height contrast, along with the 0.65 nm lateral periodicity.

The evaporation of Ag on Si(111) 7×7 , as shown on the right half of Figure 2, results in a honeycomb structure that is indistinguishable from the $\sqrt{3}$ Si phase on Ag(111). Atomically resolved STM topography images, as in Figure 2e ($V_{\text{sample}} = 0.75$ V), exhibit a 0.65 ± 0.02 nm periodicity (*i.e.*, 0.36 ± 0.01 nm apparent interatomic spacing) and a sublattice inequivalence that closely resembles Figure 2c. The line profile in Figure 2f reinforces this similarity in lateral dimensions. The observed periodicity is both consistent with the HCT literature^{27,36} and experimentally indistinguishable from that of the $\sqrt{3}$ phase (*i.e.*, Figure 2d), despite the significantly different accepted structures for

$\sqrt{3}$ -silicene and HCT (see Figure S1, Supporting Information). The Fourier transforms, shown in the insets of Figure 2c,e, further confirm the materials' structural isomorphism through their coincidence throughout k -space. Similarly indistinguishable images at various biases are presented in Figure S1 (Supporting Information). On a larger scale (Figure 2g), we observe complete coverage of HCT on Si(111), where HCT domains and islands are confined within the Si(111) terraces. The line profile of Figure 2h shows step heights of 0.31 nm, which is expected for HCT capping monolayer Si(111) steps. Furthermore, significant similarities are also encountered in the structure of domain boundaries and electronic signature of these systems (discussed further in Figure S4, Supporting Information).

To summarize these STM results, we have confirmed a $\sqrt{3}$ surface ordering when depositing Ag onto Si(111) that is consistent with numerous past studies. This $\sqrt{3}$ structure forms uniformly across the entire surface (excess deposition results in the formation of Ag islands). After Si is deposited onto Ag(111), an identical $\sqrt{3}$ surface ordering results in isolated domains with variable thickness. Our initial hypothesis is that we are growing domains of crystalline sp^3 Si on Ag(111), which are capped with the same Ag-induced reconstruction as is observed for Ag deposition on Si(111). The step-heights for Si on Ag(111), as indicated in Figure 2b, are identical to the (111) interplanar spacing

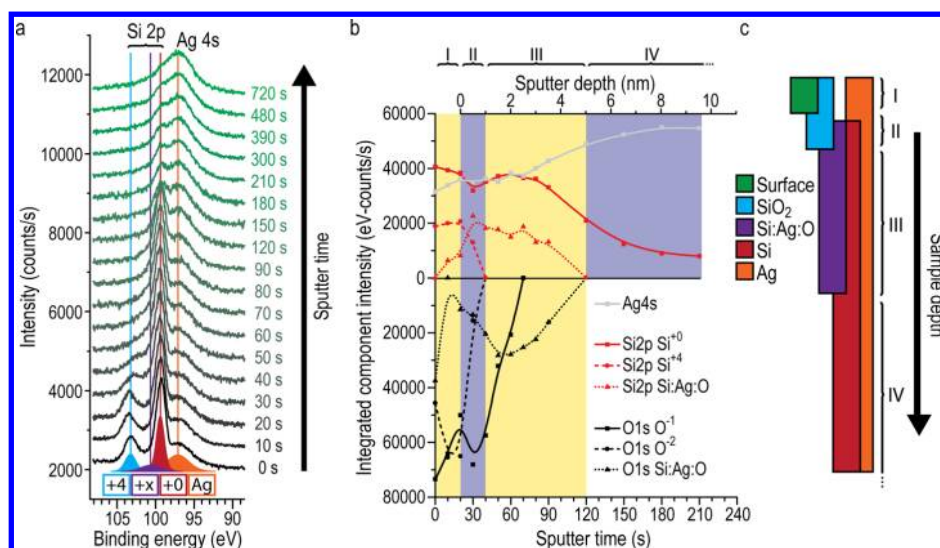


Figure 3. (a) Depth-profiled XPS spectra of the Si 2p peak acquired on the $\sqrt{3}$ phase for Si on Ag(111), demonstrating the variation in Si concentration and chemical environment versus sample depth. Schematic peak fit components are indicated. Note the presence of a Si shoulder following 720 s of sputtering, which corresponds to a non-negligible Si concentration at depth of 36 nm below the surface. (b) Plot of integrated peak intensity for fitted components of the XPS depth profile, illustrating the variation in composition for increasing sputter time (*i.e.*, sample depth). As marked, region I corresponds to a low energy sputter, region II indicates the SiO₂ layer, region III is characterized by the coexistence of intermediate oxidation species, and region IV denotes the removal of oxides and exposure of the silver bulk. These regions are depicted schematically in (c). Most significantly, we note the large amount of subsurface silicon, demonstrating significant intermixing between Si and Ag.

in diamond cubic silicon. Furthermore, the substrate provides a reservoir of Ag atoms that modify the topmost surface of the domains to a $\sqrt{3}$ structure, yielding a plausible explanation for the identical $\sqrt{3}$ geometries.

Despite the striking similarities encountered in STM, the lack of chemical information requires the use of other tools to convincingly elucidate the nature of these similar structures. XPS is a highly surface-sensitive technique, capable of identifying both the elemental species present and their chemical environment. Additionally, the subsurface composition can be probed through XPS depth profiling, wherein an Ar⁺ ion beam is used to ablate the surface material. We employed XPS depth profiling to elucidate the chemical composition of the $\sqrt{3}$ phase, using 200 eV Ar⁺ ions to examine the extremely near-surface characteristics followed by 500 eV sputter energy to probe the subsurface region. Following UHV preparation and characterization, the $\sqrt{3}$ phase sample was transported in ambient for XPS measurements. Ambient exposure will lead to the formation of a native oxide (~ 1 nm thick), but the presence of $\sqrt{3}$ phase domains with thicknesses greater than 1 nm suggest that a significant amount of Si will survive ambient exposure unoxidized. Survey spectra (shown in Figure S5, Supporting Information) of the sample surface show only peaks attributed to Ag, Si, O, and adventitious C. The Si 2p peak (Figure 3a) is shown to vary significantly with sample depth, consistent with significant changes in the local chemical environment of the Si atoms. At the surface (*i.e.*, sputter time of 0 s), this peak can be fit by components corresponding to

Si⁰⁺, Si⁴⁺, and an intermediate peak attributable to intermediate oxidation states³⁷ or Si–Ag interaction,³⁸ as well as a component for the nearby Ag 4s peak. These results are similar to those obtained *in situ* on lower temperature growth silicene phases.³⁹ The Si⁴⁺ component is consistent with the formation of a native SiO₂ layer, as expected following the ambient exposure of a bulk Si surface.

Figure 3b shows a depth profile obtained by plotting the integrated Ag 4s, Si 2p, and O 1s fitted peak intensities versus the calibrated Ag sputter rate. In the low-energy sputter stage (region I), we observe relative shifts in O component areas, but no significant modification to the Ag or Si components. This observation is consistent with the removal of adsorbed H₂O and other contaminants, along with ion-induced damage of the top oxide layer. Increasing the sputter energy to 500 eV, we observe the extinction of the Si⁴⁺ and O²⁻ components in region II, consistent with the removal of a SiO₂ layer at the surface. As will be shown below, AFM and Raman data suggest that any remaining $\sqrt{7}$ phase is completely oxidized and, therefore, likely removed in this step as well. In region III, we observe the removal of the Si component associated with HCT or intermediate oxidation species. This observation is interpreted as the complete removal of the $\sqrt{3}$ phase islands, along with accompanying Si precipitates, wherein the intermediate oxidation species are associated with oxidation at grain boundaries and the Ag–Si interface. Further sputtering into region IV produces a decrease in the Si⁰⁺ component intensity, which persists as a shoulder on the Ag 4s peak even at the maximum depth at

which data were collected (36 nm). This persistence of the Si^{0+} component intensity indicates appreciable Si dissolution within the near-surface region of the Ag, reinforcing our assessment that Ag and Si undergo non-negligible intermixing. The depth-dependent evolution of the Si 2s spectra corroborates these data (see Figure S5, Supporting Information). The phases present in Regions I–IV, as inferred through XPS, are schematically depicted in Figure 3c. Notably, these data suggest that a significant amount of Si escapes oxidation following ambient exposure.

In order to further explore the relationship between the two systems, additional characterization of the $\sqrt{3}$ phase structure is necessary. Cross-sectional TEM samples were prepared using focused ion beam (FIB) milling, allowing us to select specific regions for microscopic analysis. Scanning electron microscope images and the details of FIB sample preparation are given in Figure S6 (Supporting Information). Bright field (BF) transmission electron micrographs, as in Figure 4a, demonstrate the stratified morphology expected for a cross-sectional sample. We immediately note the presence of relatively bright, planar features at the interface between the Ag substrate and Pt capping layers. These planar features are tentatively identified as regions of the $\sqrt{3}$ phase, since these features correspond to the faceted domains that were selected during the FIB sample preparation. A magnified image, shown in Figure 4b, shows a shallow region of $\sqrt{3}$ phase, ~ 1 nm in thickness, connecting two larger $\sqrt{3}$ phase domains. The significant variation in $\sqrt{3}$ phase thickness is the result of the high Si dose (>5 ML), which ensured ambient survival. High-resolution BF images, as in Figure 4c, illustrate the abrupt interface between the Ag substrate and $\sqrt{3}$ phase. Within this frame, selected area diffraction patterns (SADP) were obtained to establish the crystalline structure of the material. Figure 4d shows the SADP obtained within the Ag substrate region, which is indexed along the Ag $[01\bar{1}]$ direction. The observed SADP is consistent with the known orientation of the Ag (111) substrate. Without additional sample rotation, a SADP was obtained from the $\sqrt{3}$ phase region, as shown in Figure 4e. The abrupt change in symmetry is consistent with the transition to distinct crystalline phase, whereas the relatively weak diffraction is due to the higher index Si $[11\bar{2}]$ zone axis. The 90° angle between the 111 and $2\bar{2}0$ diffraction spots, as well as the measured 0.32 nm Si(111) and 0.21 nm Si($2\bar{2}0$) interplanar spacing, are consistent with this structure assignment. We obtain additional chemical information through scanning transmission electron microscopy using a high-angle annular diffraction detector (Figure 4f), which is sensitive to differences in the atomic number. This z-contrast allows us to compositionally distinguish the $\sqrt{3}$ phase region from its surrounding Ag substrate and Pt capping layer, confirming the chemically

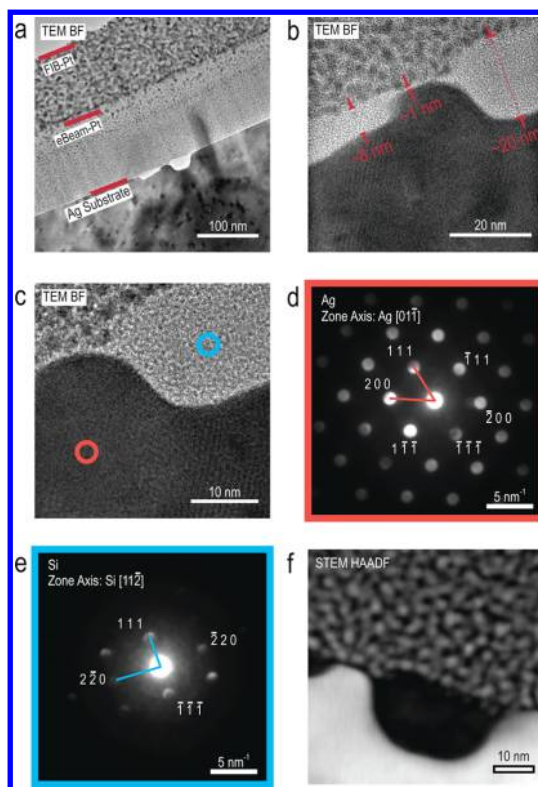


Figure 4. (a) Wide view, bright field TEM image of the cross-sectional sample, with the protective Pt capping layers and Ag substrate indicated. (b) Bright field TEM image showing several of the contrasting features, which are identified as the Si $\sqrt{3}$ phase. (c) High-resolution bright field TEM image demonstrating the abrupt structure of the Si/Ag interface. The circles indicate regions where SADP were obtained. (d) SADP obtained from the orange circle in (c), which is indexed to the Ag $[01\bar{1}]$ zone axis. (e) SADP obtained in the blue circle shown in (c), at the same sample orientation as (d), which corresponds to a Si $[11\bar{2}]$ zone axis. (f) STEM HAADF detector image, which reveals the significant z-contrast between the Si $\sqrt{3}$ phase, the Ag substrate, and the Pt capping layer.

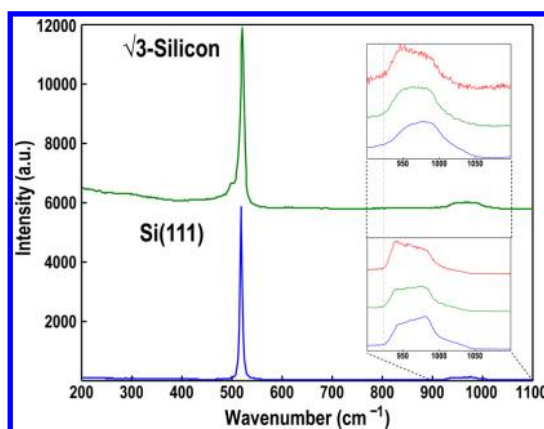


Figure 5. Raman spectra (514 nm excitation) for the $\sqrt{3}$ phase for Si on Ag(111) (top) and a bulk Si(111) wafer (bottom) both show a characteristic peak at 520 cm^{-1} for the TO phonon of sp^3 -bonded silicon. The small shoulder in the $\sqrt{3}$ phase spectrum at 495 cm^{-1} is consistent with the formation of a thin, ordered silicon oxide layer. Insets show the 2TO phonon modes for both materials at an excitation wavelength of 442 nm (blue curve), 514 nm (green curve), and 633 nm (red curve), revealing their similar dispersive characteristics.

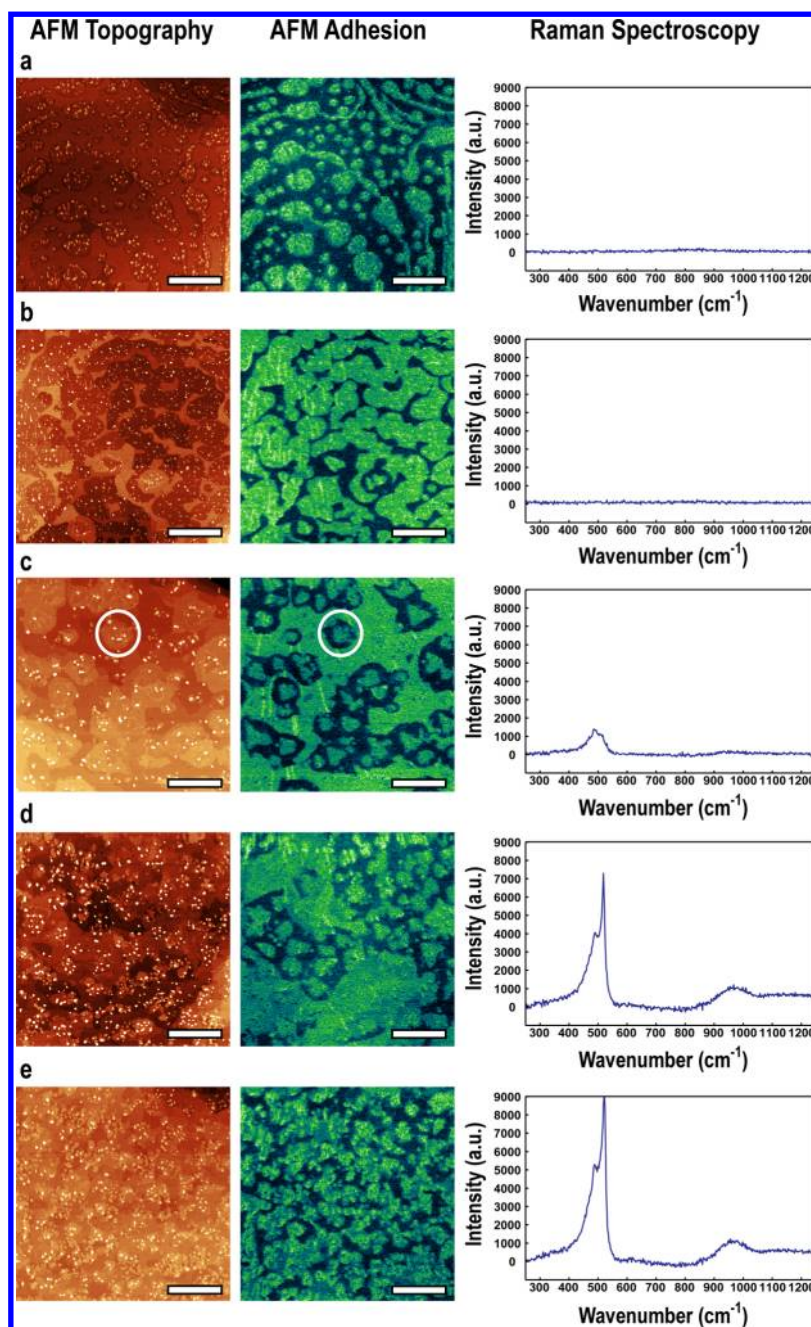


Figure 6. Series of AFM topography and adhesion images and correlated Raman spectra for varying silicon coverage on Ag(111) (scale bars = 500 nm). Green regions in the AFM adhesion indicate the $\sqrt{7}$ phase for Si on Ag(111) at low coverage (a) and nearly full coverage (b), both demonstrating negligible Raman scattering. (c) Nucleation of $\sqrt{3}$ phase islands (circled in the AFM topography and adhesion images) begins after full monolayer $\sqrt{7}$ phase is reached. The $\sqrt{3}$ phase growth depletes silicon from the surrounding $\sqrt{7}$ phase regions, leading to encircling patches of bare Ag; (d) and (e) illustrate further precipitation of $\sqrt{3}$ phase and the associated Raman mode for bulk silicon at 520 cm^{-1} with an associated shoulder at 495 cm^{-1} attributed to a thin, ordered silicon oxide.

distinct nature of these phases. The persistent crystal-line structure of the $\sqrt{3}$ phase *ex situ* suggests the viability of this ultrathin Si phase in electronic applications, where the formation of a passivating surface oxide facilitates transfer from the Ag growth substrate.

However, in order to verify the properties of the $\sqrt{3}$ phase on a larger scale, Raman spectroscopy was employed to provide spatially resolved information related to both the structure and composition of the

sample. Raman spectra acquired *ex situ* on the $\sqrt{3}$ phase exhibit an intense peak at $\sim 520\text{ cm}^{-1}$, as shown in the top curve in Figure 5. This peak coincides with the ubiquitous TO phonon mode in bulk Si (bottom Figure 5). The location, in addition to the narrow line width ($<10\text{ cm}^{-1}$) of the peak at 520 cm^{-1} , indicates a phase of highly ordered diamond cubic crystal structure. A small shoulder at 495 cm^{-1} is also observed for the $\sqrt{3}$ phase and is attributed to locally ordered

silicon oxide;⁴⁰ its increased prominence with respect to the 520 cm^{-1} peak can be explained by the significantly enhanced volume fraction of oxide in the $\sqrt{3}$ phase sample. The presence of Si–O species is shown in Figure 3, and a similar sharp Raman peak at 495 cm^{-1} is frequently observed in previous studies of locally ordered silicon oxides.^{40–42} The $\sqrt{3}$ phase also shows modes from $900\text{ cm}^{-1} - 1100\text{ cm}^{-1}$ (Figure 3 inset) consistent with second-order transverse optical (TO) scattering modes in crystalline silicon.⁴³ The behavior of these modes at varying excitation energy is significant in that the relative intensities of the constituent 2TO(W) and 2TO(L) phonons vary with laser energy causing the shift in observed peak asymmetry.⁴⁴ Being associated with phonons out of the (111) planes, we note that minor spectral broadening of these modes is expected for the $\sqrt{3}$ phase sample due to confinement in the vertical direction.⁴⁵ Finally, the $\sqrt{3}$ phase demonstrates similar resonant Raman scattering to bulk silicon.⁴³ Significantly, these collective results indicate the survival of bulk crystalline Si modes in air without extrinsic encapsulation.

As discussed above, the Raman spectrum shown in Figure 5 was taken on a thicker $\sqrt{3}$ phase; to explore the limit of thinner layers, we prepared a sample with a concentration gradient ranging from submonolayer to slightly higher than a single monolayer. By correlating STM with *ex situ* AFM, we were able to identify and independently address regions of various silicon phases with Raman spectroscopy. Figure 6 illustrates increasing $\sqrt{7}$ phase coverage to nearly a full monolayer (Figure 6a,b) and the subsequent precipitation of $\sqrt{3}$ phase islands (Figure 6c–e). As seen in Figure 6c–e (see also Figure 7), the precipitation of the $\sqrt{3}$ phase apparently depletes silicon from the neighboring $\sqrt{7}$ phase, returning it to a nearly pure Ag surface. The precipitation of the $\sqrt{3}$ phase coincides with the emergence of a nonzero Raman signature (Figure 6c). Initially, the signature peak appears as a small convolution of two peaks near 495 and 520 cm^{-1} . As the $\sqrt{3}$ phase coverage is increased, the intensity of both modes increase, albeit disproportionately, with the 520 cm^{-1} peak rising faster. Precipitation of the $\sqrt{3}$ phase generally does not yield homogeneous monolayer regions and thus Figure 6d and 5e are likely indicative of 1–4 atomic layers, approaching the 2D limit of bulk silicon.

Spectroscopic evidence of bulk-like vibrational modes upon the precipitation of the $\sqrt{3}$ phase confirms the early assumption that the $\sqrt{3}$ phase is comprised of diamond cubic Si(111). With that in mind, the early stages of the $\sqrt{3}$ phase precipitation then provide a window to the extreme 2D limit of bulk crystalline Si. Figure 7a shows an AFM image of just such a situation; islands of the $\sqrt{3}$ phase (green) can be seen surrounded by Ag (blue) in the adhesion signal (Figure 7b) in the early stages of precipitation. The $\sqrt{3}$ phase is identified by its polyhedral faceted shape, secondary monatomic

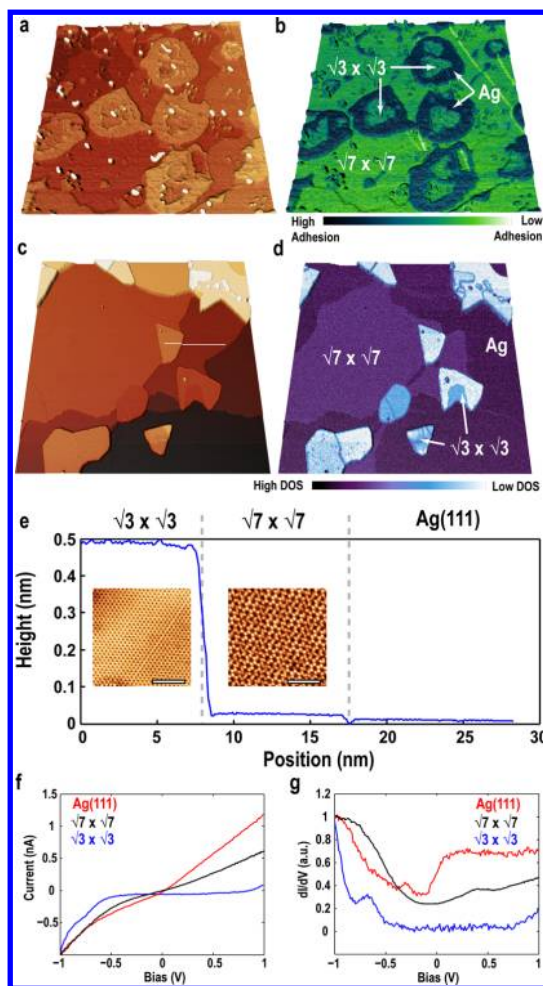


Figure 7. (a) AFM topography image and (b) adhesion signal image of neighboring $\sqrt{3}$ phase and $\sqrt{7}$ phase domains on Ag(111) (image size = $2 \times 2\ \mu\text{m}^2$). (c) STM topography image and (d) differential tunneling conductance (dI/dV) image of neighboring $\sqrt{3}$ phase and $\sqrt{7}$ phase domains (image size = $100 \times 75\ \text{nm}^2$, $V_{\text{sample}} = 2.0\ \text{V}$, $I_t = 400\ \text{pA}$, acquired at 4 K). The close proximity of these two phases suggests that Si mass transport occurs from the $\sqrt{7}$ phase to drive the sp^3 -bonded Si growth in the $\sqrt{3}$ phase. (e) STM topography line profile obtained across white line in (c). Insets illustrate characteristic atomic-scale structure of each region (scale bars = 4 nm). (f) I – V and (g) dI/dV obtained on the indicated regions, illustrating the significant change in electronic character for the semiconducting $\sqrt{3}$ phase versus the metallic Ag(111) and $\sqrt{7}$ phase.

height islands, and envelopment by the surrounding silver, indicating silicon depletion from the $\sqrt{7}$ phase. We further note that the $\sqrt{7}$ phase region generally grows to full surface coverage before the precipitation of the $\sqrt{3}$ phase, whereupon bare Ag is once again observed. Following heavy Si doses (*e.g.*, >5 monolayer), we occasionally observe buried island or planar void features in the STM topography, similar to the segregation-driven growth of bilayer graphene films on Ir(111).⁴⁶ Previous studies have noted that noble metal substrates induce the crystallization of amorphous Ge films⁴⁷ suggesting that a combination of surface transport and segregation contribute toward growth.

Correlating the *ex situ* AFM to STM (Figure 7c,d), it is particularly interesting that the *in situ* measurements indicate little height variation between the $\sqrt{7}$ phase and Ag, as illustrated in the line profile, while the $\sqrt{3}$ phase is clearly physically elevated above both the $\sqrt{7}$ phase and Ag. Furthermore, the differential tunneling conductance map of Figure 7d indicates that all materials are electronically distinct; I/V and dI/dV point spectra (Figure 7f,g) clearly show the progression from metallic (Ag), to weakly metallic ($\sqrt{7}$ phase), to semiconducting ($\sqrt{3}$ phase). These results show that the $\sqrt{3}$ phase retains semiconducting behavior down to the single layer limit. However, additional studies are required to address the effect of increased confinement, as well as that of the Ag-induced reconstruction, which will likely result in fundamentally interesting modifications to the transport properties.^{48,49}

CONCLUSION

In conclusion, we have completed an extensive investigation of ultrathin Si on Ag(111). STM studies of Si deposition on Ag(111) revealed multiple single-layer surface phases with the $\sqrt{3}$ phase showing energetic favorability. The growth of the $\sqrt{3}$ phase

was controlled from single-layer platelets to multilayer regions, all of which formed as isolated domains rather than uniformly covering the surface. Guided by previous studies of Ag deposition on Si(111), we demonstrated *via* STM that the $\sqrt{3}$ phase was structurally identical to the HCT surface reconstruction (described by HCT and IET models). To understand this observation, we studied the $\sqrt{3}$ phase system *ex situ*. Cross-sectional TEM images show that the $\sqrt{3}$ phase adopts a planar subsurface morphology and remains crystalline below a surface oxide following ambient exposure. Raman spectroscopy indicates the persistence of sp^3 crystalline silicon despite the concomitant observation of silicon oxide *via* XPS. Furthermore, the appearance of bulk Raman scattering modes is directly correlated to the precipitation of $\sqrt{3}$ phase. These observations indicate that a semiconducting sp^3 bonded monolayer of silicon is the most favorable allotrope in the 2D limit. Since these Si nanosheets retain a bulk-like semiconducting electronic signature even at the ultimate thickness limit, they can likely overcome the limitations caused by the gapless nature of sp^2 -bonded 2D materials in a platform inherently compatible with extant Si processing chemistries.

METHODS

$\sqrt{3}$ phase silicon nanosheets and HCT synthesis and analysis took place in a Omicron VT-STM and a Omicron 4K STM equipped with separate sample preparation and analysis chambers. In the preparation chamber (base pressure $<5 \times 10^{-11}$ mBar), the Ag(111) single crystal substrate (Matek, 99.999%, $<0.1^\circ$ miscut) was prepared *via* repeated cycles of room temperature Ar sputtering (1 kV, 10^{-5} mBar) and annealing at 550 °C to generate a flat, clean surface (verified with STM imaging). Si phases were grown *via* UHV electron beam evaporation (Omicron Nanotechnology) from a polycrystalline Si source rod (ESPI metals, 1.5 mm dia., 99.9999%) onto the resistively heated Ag(111) substrate at temperatures of 200–360 °C. Generally, 800 V accelerating voltage and 17 mA emission current produced a steady flux, with negligible rise in chamber pressure (*i.e.*, $<10^{-10}$ mBar). Si was deposited at a rate of ~ 0.05 ML/min (verified with STM imaging) for 30–90 min.

A clean Si(111) 7×7 surface was prepared from an As-doped Si(111) wafer (Virginia Semiconductor, 2–3 m Ω -cm) through cycles of direct current heating to 1250 °C and gradual cooling to 950 °C. HCT was synthesized through electron beam evaporation of Ag (ESPI metals, 1.5 mm dia., 99.999%), while the substrate was maintained at 25–500 °C, followed by annealing to 300–500 °C.

STM images were obtained in the analysis chamber (base pressure $<2 \times 10^{-12}$ mBar) in constant current mode using electrochemically etched W tips at 55 K, unless noted otherwise. Simultaneous scanning tunneling spectroscopy dI/dV mapping was obtained by applying a small periodic modulation to the sample bias and isolating the current signal with a Stanford Research Systems SR830 lock-in amplifier (at 10 kHz with $V_{\text{mod}} = 30$ mV zero-to-peak voltage). Ag(111) reference spectra were periodically taken to confirm tip consistency.

XPS spectra were acquired on a Thermo Scientific ESCALAB 250 Xi, using a monochromated Al K α source and an Ar⁺ ion gun for depth profiling. The depth profile was quantified using a calibrated etch rate. TEM samples were prepared using an FEI Helios Nanolab SEM/FIB, followed by precision thinning in a Fischione NanoMill *via* Ar⁺ ion sputtering. TEM/STEM and EDS data were acquired using a JEOL JEM-2100F with a double

tilt holder. AFM images were obtained using a Bruker Nanoscope 7 in PeakForce mode. Raman spectra were taken with a Renshaw Confocal Raman system with 442, 514, and 633 nm lasers.

Conflict of Interest: The authors declare no competing financial interest.

Acknowledgment. We thank Dr. J. D. Wood (Northwestern University) and Prof. K. E. Newman (University of Notre Dame) for discussions and B. D. Myers and Dr. S.-Y. Li (Northwestern University) for assistance with FIB and TEM. This work was performed at the Center for Nanoscale Materials, a U.S. Department of Energy, Office of Science, Office of Basic Energy Sciences User Facility, under Contract No. DE-AC02-06CH11357. B.K. acknowledges support from a National Science Foundation Graduate Research Fellowship (DGE-0824162). This work was also supported by the U.S. Department of Energy SISGR Contract No. DE-FG02-09ER16109.

Supporting Information Available: Structural models of the $\sqrt{3}$ phase and HCT, bias-dependent STM image comparison of $\sqrt{3}$ phase and HCT, images of lower growth temperature phases, STM and AFM images of high Si coverage morphology, STM image comparison of $\sqrt{3}$ phase and HCT defects, $\sqrt{3}$ phase and HCT STS comparison, complete XPS data set, and TEM sample preparation details. This material is available free of charge *via* the Internet at <http://pubs.acs.org>.

REFERENCES AND NOTES

- Geim, A. K.; Novoselov, K. S. The Rise of Graphene. *Nat. Mater.* **2007**, *6*, 183–191.
- Huang, P. Y.; Ruiz-Vargas, C. S.; van der Zande, A. M.; Whitney, W. S.; Levendorf, M. P.; Kevek, J. W.; Garg, S.; Alden, J. S.; Hustedt, C. J.; Zhu, Y.; et al. Grains and Grain Boundaries in Single-Layer Graphene Atomic Patchwork Quilts. *Nature* **2011**, *469*, 389–392.
- Berger, C.; Song, Z.; Li, X.; Wu, X.; Brown, N.; Naud, C.; Mayou, D.; Li, T.; Hass, J.; Marchenkov, A. N.; et al.

- Electronic Confinement and Coherence in Patterned Epitaxial Graphene. *Science* **2006**, *312*, 1191–1196.
4. Yu, Q.; Jauregui, L. A.; Wu, W.; Colby, R.; Tian, J.; Su, Z.; Cao, H.; Liu, Z.; Pandey, D.; Wei, D.; et al. Control and Characterization of Individual Grains and Grain Boundaries in Graphene Grown by Chemical Vapour Deposition. *Nat. Mater.* **2011**, *10*, 443–449.
 5. Yang, W.; Chen, G.; Shi, Z.; Liu, C.-C.; Zhang, L.; Xie, G.; Cheng, M.; Wang, D.; Yang, R.; Shi, D.; et al. Epitaxial Growth of Single-Domain Graphene on Hexagonal Boron Nitride. *Nat. Mater.* **2013**, *2*, 1–6.
 6. Najmaei, S.; Liu, Z.; Zhou, W.; Zou, X.; Shi, G.; Lei, S.; Yakobson, B. I.; Idrobo, J.-C.; Ajayan, P. M.; Lou, J. Vapour Phase Growth and Grain Boundary Structure of Molybdenum Disulphide Atomic Layers. *Nat. Mater.* **2013**, *12*, 754–759.
 7. Chhowalla, M.; Shin, H. S.; Eda, G.; Li, L.-J.; Loh, K. P.; Zhang, H. The Chemistry of Two-Dimensional Layered Transition Metal Dichalcogenide Nanosheets. *Nat. Chem.* **2013**, *5*, 263–275.
 8. Castro Neto, A. H.; Peres, N. M. R.; Novoselov, K. S.; Geim, A. K. The Electronic Properties of Graphene. *Rev. Mod. Phys.* **2009**, *81*, 109–162.
 9. Takeda, K.; Shiraishi, K. Theoretical Possibility of Stage Corrugation in Si and Ge Analogs of Graphite. *Phys. Rev. B* **1994**, *50*, 14916.
 10. Cahangirov, S.; Topsakal, M.; Aktürk, E.; Şahin, H.; Ciraci, S. Two- and One-Dimensional Honeycomb Structures of Silicon and Germanium. *Phys. Rev. Lett.* **2009**, *102*, 236804.
 11. Guzmán-Verri, G.; Lew Yan Voon, L. Electronic Structure of Silicon-Based Nanostructures. *Phys. Rev. B* **2007**, *76*, 075131.
 12. Ni, Z.; Liu, Q.; Tang, K.; Zheng, J.; Zhou, J.; Qin, R.; Gao, Z.; Yu, D.; Lu, J. Tunable Bandgap in Silicene and Germanene. *Nano Lett.* **2012**, *12*, 113–118.
 13. Ezawa, M. Valley-Polarized Metals and Quantum Anomalous Hall Effect in Silicene. *Phys. Rev. Lett.* **2012**, *109*, 055502.
 14. Liu, C.-C.; Feng, W.; Yao, Y. Quantum Spin Hall Effect in Silicene and Two-Dimensional Germanium. *Phys. Rev. Lett.* **2011**, *107*, 076802.
 15. Aufray, B.; Kara, A.; Vizzini, S.; Oughaddou, H.; Léandri, C.; Ealet, B.; Le Lay, G. Graphene-like Silicon Nanoribbons on Ag(110): A Possible Formation of Silicene. *Appl. Phys. Lett.* **2010**, *96*, 183102.
 16. Vogt, P.; De Padova, P.; Quaresima, C.; Avila, J.; Frantzeskakis, E.; Asensio, M.; Resta, A.; Ealet, B.; Le Lay, G. Silicene: Compelling Experimental Evidence for Graphene-Like Two-Dimensional Silicon. *Phys. Rev. Lett.* **2012**, *108*, 155501.
 17. Feng, B.; Ding, Z.; Meng, S.; Yao, Y.; He, X.; Cheng, P.; Chen, L.; Wu, K. Evidence of Silicene in Honeycomb Structures of Silicon on Ag(111). *Nano Lett.* **2012**, *12*, 3507–3511.
 18. Meng, L.; Wang, Y.; Zhang, L.; Du, S.; Wu, R.; Li, L.; Zhang, Y.; Li, G.; Zhou, H.; Hofer, W. A.; et al. Buckled Silicene Formation on Ir(111). *Nano Lett.* **2013**, *13*, 685–690.
 19. Fleurence, A.; Friedlein, R.; Ozaki, T.; Kawai, H.; Wang, Y.; Yamada-Takamura, Y. Experimental Evidence for Epitaxial Silicene on Diboride Thin Films. *Phys. Rev. Lett.* **2012**, *108*, 245501.
 20. Chen, L.; Liu, C.-C.; Feng, B.; He, X.; Cheng, P.; Ding, Z.; Meng, S.; Yao, Y.; Wu, K. Evidence for Dirac Fermions in a Honeycomb Lattice Based on Silicon. *Phys. Rev. Lett.* **2012**, *109*, 056804.
 21. Feng, B.; Li, H.; Liu, C.; Shao, T.-N.; Cheng, P.; Yao, Y.; Meng, S.; Chen, L.; Wu, K. Observation of Dirac Cone Warping and Chirality Effects in Silicene. *ACS Nano* **2013**, *7*, 9049–9054.
 22. Chen, L.; Li, H.; Feng, B.; Ding, Z.; Qiu, J.; Cheng, P.; Wu, K.; Meng, S. Spontaneous Symmetry Breaking and Dynamic Phase Transition in Monolayer Silicene. *Phys. Rev. Lett.* **2013**, *110*, 085504.
 23. De Padova, P.; Vogt, P.; Resta, A.; Avila, J.; Razado-Colambo, I.; Quaresima, C.; Ottaviani, C.; Olivieri, B.; Bruhn, T.; Hirahara, T.; et al. Evidence of Dirac Fermions in Multilayer Silicene. *Appl. Phys. Lett.* **2013**, *102*, 163106.
 24. Chen, L.; Feng, B.; Wu, K. Observation of a Possible Superconducting Gap in Silicene on Ag(111) Surface. *Appl. Phys. Lett.* **2013**, *102*, 081602.
 25. Le Lay, G. Physics and Electronics of the Noble-Metal/Elemental-Semiconductor Interface Formation: a Status Report. *Surf. Sci.* **1983**, *132*, 169–204.
 26. Ding, Y.; Chan, C.; Ho, K. Structure of the $(\sqrt{3} \times \sqrt{3}) R30^\circ$ Ag/Si (111) Surface from First-Principles Calculations. *Phys. Rev. Lett.* **1991**, *67*, 1454–1458.
 27. Aizawa, H.; Tsukada, M.; Sato, N.; Hasegawa, S. Asymmetric Structure of the Si (111)- $\sqrt{3} \times \sqrt{3}$ -Ag Surface. *Surf. Sci.* **1999**, *429*, 509–514.
 28. Marks, L. D.; Bengu, E.; Collazo-Davila, C.; Grozea, D.; Landree, E.; Leslie, C.; Sinkler, W. Direct Methods for Surfaces. *Surf. Rev. Lett.* **1998**, *05*, 1087–1106.
 29. Sato, N.; Takeda, S.; Nagao, T.; Hasegawa, S. Electron Standing Waves on the Si (111)- $(\sqrt{3} \times \sqrt{3})$ Ag Surface. *Phys. Rev. B* **1999**, *59*, 2035–2039.
 30. Mochizuki, I.; Negishi, R.; Shigeta, Y. Strain Induced Modification of Quasi-Two-Dimensional Electron Gas State on $\sqrt{3} \times \sqrt{3}$ -Ag Structure. *J. Appl. Phys.* **2010**, *107*, 084317.
 31. Theobald, J. A.; Oxtoby, N. S.; Phillips, M. A.; Champness, N. R.; Beton, P. H. Controlling Molecular Deposition and Layer Structure with Supramolecular Surface Assemblies. *Nature* **2003**, *424*, 1029–1031.
 32. Porter, T.; Chang, C.; Tsong, I. Si (111)- $(\sqrt{3} \times \sqrt{3}) R30^\circ$ Ag Surface Structure Studied by Impact-Collision Ion-Scattering Spectrometry. *Phys. Rev. Lett.* **1988**, *60*, 1739–1742.
 33. Vlieg, E.; Fontes, E.; Patel, J. Structure Analysis of Si (111)- $(\sqrt{3} \times \sqrt{3}) R30^\circ$ /Ag Using X-Ray Standing Waves. *Phys. Rev. B* **1991**, *43*, 7185–7193.
 34. Nagao, T.; Hasegawa, S.; Tsuchie, K.; Ino, S. Structural Phase Transitions of Si (111)- $(\sqrt{3} \times \sqrt{3}) R30^\circ$ /Au: Phase Transitions in Domain-Wall Configurations. *Phys. Rev. B* **1998**, *57*, 100–109.
 35. Vogt, P.; Capiod, P.; Berthe, M. Synthesis and Electrical Conductivity of Multilayer Silicene. *Appl. Phys. Lett.* **2014**, *021602*.
 36. Sweetman, A.; Stannard, A.; Sugimoto, Y.; Abe, M.; Morita, S.; Moriarty, P. Simultaneous Noncontact AFM and STM of Ag:Si(111)- $(\sqrt{3} \times \sqrt{3}) R30^\circ$. *Phys. Rev. B* **2013**, *87*, 075310.
 37. Yau, S.; Arendt, M.; Bard, A. J.; Evans, B. Study of the Structure and Chemical Nature of Porous Si and Siloxene by STM, AFM, XPS, and LIMA. *J. Electrochem. Soc.* **1994**, *141*, 402–409.
 38. Schmitsdorf, R.; Mönch, W. Oxidation of Silver-Passivated Si(111):Ag- $(\sqrt{3} \times \sqrt{3}) R30^\circ$ Surfaces. *Surf. Sci.* **1996**, *354*, 322–326.
 39. Molle, A.; Grazianetti, C.; Chiappe, D.; Cinquanta, E.; Cianci, E.; Tallarida, G.; Fanciulli, M. Hindering the Oxidation of Silicene with Non-Reactive Encapsulation. *Adv. Funct. Mater.* **2013**, *23*, 4340–4344.
 40. Galeener, F.; Barrio, R.; Martinez, E.; Elliott, R. Vibrational Decoupling of Rings in Amorphous Solids. *Phys. Rev. Lett.* **1984**, *53*, 2429–2432.
 41. Galeener, F. L.; Mikkelsen, J. C. Raman Studies of the Thermal Oxide of Silicon. *Solid State Commun.* **1981**, *37*, 719–723.
 42. Galeener, F. Planar Rings in Glasses. *Solid State Commun.* **1982**, *44*, 1037–1040.
 43. Renucci, J.; Tyte, R.; Cardona, M. Resonant Raman Scattering in Silicon. *Phys. Rev. B* **1975**, *11*, 3885–3896.
 44. Tanino, H.; Kuprin, A.; Deai, H.; Koshida, N. Raman Study of Free-Standing Porous Silicon. *Phys. Rev. B. Condens. Matter* **1996**, *53*, 1937–1947.
 45. Campbell, I.; Fauchet, P. The Effects of Microcrystal Size and Shape on the One Phonon Raman Spectra of Crystalline Semiconductors. *Solid State Commun.* **1986**, *58*, 739–741.
 46. Nie, S.; Walter, A. L.; Bartelt, N. C.; Starodub, E.; Bostwick, A.; Rotenberg, E.; McCarty, K. F. Growth from below: Graphene Bilayers on Ir(111). *ACS Nano* **2011**, *5*, 2298–2306.

47. Tan, Z.; Heald, S.; Rapposch, M.; Bouldin, C.; Woicik, J. Gold-Induced Germanium Crystallization. *Phys. Rev. B* **1992**, *46*, 9505–9510.
48. Gomes, K. K.; Mar, W.; Ko, W.; Guinea, F.; Manoharan, H. C. Designer Dirac Fermions and Topological Phases in Molecular Graphene. *Nature* **2012**, *483*, 306–310.
49. Polini, M.; Guinea, F.; Lewenstein, M.; Manoharan, H. C.; Pellegrini, V. Artificial Honeycomb Lattices for Electrons, Atoms and Photons. *Nat. Nanotechnol.* **2013**, *8*, 625–633.